Delft University of Technology

Mapping spatial organization of in vitro neuronal networks using high-content imaging

Casotto, Angelica; Frias, Cátia P.; Joosten, Myta; Teurlings, Selina M.W.; Schonewille, Martijn; van Woerden, Geeske M.; Zwanikken, Jos W.; Meijer, Dimphna H.

Important note
To cite this publication, please use the final published version (if applicable).
Please check the document version above.

scientific reports

Check for updates

OPEN

Mapping spatial organization of in vitro neuronal networks using high-content imaging

Angelica Casotto[1,2,4], Cátia P. Frias[1,4], Myta Joosten[1], Selina M. W. Teurlings[1,2], Martijn Schonewille[2], Geeske M. van Woerden[2,3], Jos W. Zwanikken[1] & Dimphna H. Meijer[1✉]

Neuronal network formation is an intricate process by which individual neurons connect into a functional circuitry. At the subcellular level, neuronal connectivity is characterized by the number, size and strength of synapses. At the cellular level, in vitro network characterization remains a challenge due to the large number of neurons involved, spreading widely across a culture dish. Here, we demonstrate a pipeline using high-content confocal microscopy and automated image analysis to study spatial organization of individual neurons in an in vitro cellular network. With this approach, we enable analysis of thousands of neurons in one well, and of multiple wells simultaneously. Using this workflow, we compared the spatial organization of primary mouse neuronal networks derived from the hippocampus, cortex and cerebellum. We also demonstrate how to extract morphological details, such as size of the nucleus and axon initial segment number, orientation and length from our data. This workflow can be applied to study underlying molecular mechanisms of circuitry formation, to assess network formation of neurons derived from mouse or human iPSC models for neurological diseases, and serve as a future platform for drug development.

Neuronal circuits constitute the core architectural framework of brain function, supporting both fundamental physiological processes and advanced cognitive functions[1,2]. The dynamics within these circuits ensure adaptation to new information, maintenance of homeostasis, and robust support of complex behaviours. Importantly, the connectivity patterns of neuronal circuits are highly organized, following specific architectural principles that are yet to be fully discovered. These principles are not only evident at the network level but are also reflected in the intrinsic properties of individual neurons. Neurons carry intrinsic, cell-type-specific programs that shape how they self-organize and interconnect. As a result, different brain regions exhibit distinct organisational structures. In the intact brain, hippocampal neurons for instance, form micro-circuits projecting from the CA3 to the CA1 region, but also display refined spatial organization within these regions[3]. Cortical neurons are known to organize into layered and columnar modules[4], and cerebellar Purkinje cells are neatly arranged into one singular layer[5]. In dissociated neuronal cultures, neurons display characteristic features as well. For instance, neurons grown in vitro spontaneously form small-world, modular networks, with strongly clustered modules of spatially proximal cells[2,6–9]. Such cultures exhibit complex patterns of growth and connectivity, where some regions become highly connected while others remain relatively less active[10]. These patterns are driven by cell-type-specific cues: for example, homophilic and heterophilic cell adhesion molecules guide the specificity of synaptic connections[11]. Recent advances in non-invasive imaging and automated analysis now allow researchers to track both structural and functional dynamics of neuronal networks over time[12,13]. For example, aggregated cultures form more resilient and locally connected networks when analysing their clustering and activity during development in cell culture dishes[14]. Disruptions in neuronal self-organization are a hallmark of various neurological disorders, making in vitro models valuable systems for investigating the principles underlying both healthy and pathological network development. Moreover, they are more accessible and easier to manipulate than in vivo systems, supporting mechanistic studies of the principles that guide neuronal network formation and dysfunction[15].

In recent years, multiple software tools have been developed to quantify neuronal cultures, allowing researchers to convert static microscope images into measurable features. This includes counting cells, measuring neurite length and assessing synaptic density (reviewed in[16]). However, complete reconstruction and analysis

[1]Department of Bionanoscience, Kavli Institute of Nanoscience, Delft University of Technology, Van Der Maasweg 9, 2629 HZ Delft, The Netherlands. [2]Department of Neuroscience, Erasmus Medical Center, Rotterdam, The Netherlands. [3]Department of Clinical Genetics, Erasmus Medical Center, Rotterdam, The Netherlands. [4]Angelica Casotto and Cátia P. Frias contributed equally to this work. ✉email: D.H.M.Meijer@tudelft.nl

nature portfolio

1

of neuronal networks remains challenging due to the large number of neurons involved, even within small culture dishes. Combining primary neuronal cell culture with high-content imaging, originally used for drug screening, would be a powerful method for studying cell populations and morphological changes at the scale of neuronal networks[17–19]. High-content imaging enables large-scale, rapid analysis of thousands of individual cells, and recent developments allow researchers to customize analysis pipelines for specific questions[20], and to perform single-cell quantifications[21]. Modern high-content imaging platforms are compatible with multi-well plates, allowing for parallel imaging of multiple conditions. These developments now enable, for instance, detailed tracking of neuronal development. In fact, high throughput imaging has been employed to characterise distinct growth dynamics across neuronal cell models. For instance chicken cerebellar granule neurons develop few, but long neurites, NT2N cells form complex networks with many connections, and rat PC12N cells undergo dynamic changes in soma number and connections over time[22]. However, these experiments were performed without taking into account the complete cellular networks in the cell culture dish.

Here, we present a pipeline using high-content confocal microscopy to gain new insights into how neurons establish in vitro cellular networks. We first describe the experimental setup compatible with high-content microscopy, and the image stitching process for analysing complete neuronal networks. We then extract information about the global and local organization of neuronal and non-neuronal cells in the cellular network. Finally, we demonstrate that this pipeline is suitable for different neuronal preparations (cerebellar, cortical and hippocampal primary neuronal cultures) and has the potential to address various biological questions, for instance on the development of the axon initial segment and neurodevelopmental biology in general.

Results

### Automated imaging workflow to visualize in vitro neuronal networks

In order to study neuronal organization in complete cell culture wells, we developed a workflow combining automated high-content imaging with automated neuronal detection of primary neuronal cultures. To this end, we plated cortical, hippocampal and cerebellar primary cells, originating from mouse brain tissue, into 24- or 96-well plates. Neurons were then fixed at 7, 10 or 14 days in vitro (DIV) and stained for markers representing different neuronal compartments or subtypes (Fig. 1A–C). For cortical and hippocampal neurons, we stained the nuclei with DAPI, the soma and dendrites with an anti-MAP2 antibody and labelled the axon initial segment (AIS) with Ankyrin-G (Ank-G) (Fig. 1A,B). Ank-G will be used in the subsequent section for neuronal cell identification. To identify Purkinje neurons in cerebellar cultures, we used an anti-Calbindin antibody (Fig. 1C). Next, the complete wells were imaged using automated high-content microscopy. For 24-well plates, 400 images at 10X magnification per well were taken, while for 96-wells, 225 images at 20X magnification per well were sufficient to cover the entire well area. The individual confocal images, which are maximum intensity projections, were then stitched together using an adapted ImageJ plugin to form a full-well image (Figs. 1D and 2A).

Automated and manual detection of neuronal and non-neuronal cells in primary networks

The stitched full-well images enable both automated and manual identification of neuronal and non-neuronal cells across different brain regions. To ensure spatial accuracy, stitching precision was assessed using positional data from the image stitching plug-in. Residual displacements were calculated as the absolute difference between the expected and aligned tile positions. Mean residual displacements (mean ± SD) were 1.49 ± 0.40 μm (DIV7), 1.78 ± 1.31 μm (DIV10), and 3.09 ± 3.37 μm (DIV14) for cortical cultures; 0.35 ± 0.28 μm (DIV7), 0.23 ± 0.05 μm (DIV10), and 0.50 ± 0.44 μm (DIV14) for hippocampal cultures; and 1.91 ± 0.82 μm (DIV14) for cerebellar cultures. We then developed an automated analysis pipeline that receives stitched images of entire wells as input, allowing us to count cells in primary neuronal networks (Fig. 2A). Neurons were identified using Ank-G, the marker for the axonal initial segment, while non-neuronal cells were defined as DAPI-positive and Ank-G negative (Fig. 3E). Classification performance was evaluated on a manually annotated subset of tiles, generating a confusion matrix (Fig. 2B) that confirmed high precision with no false positives for neuronal cells, although some AnkG-weak neurons were misclassified as non-neuronal. The automated measurements of cell diameter were also consistent with manual analyses (Fig. 2C,D). Across all time points, we detected approximately 20,000 neurons per well in cortical cultures and 4,000 neurons in hippocampal cultures. Neuronal numbers remained stable between DIV7 and DIV14 in both culture types, suggesting consistent neuronal survival (Fig. 3A–D). In contrast, non-neuronal cell numbers showed a trend toward an increase over time, rising from 56,000 to 75,000 in cortical wells and from 5000 to 9000 in hippocampal wells. This rise might reflect the regular cell proliferation programs in non-neuronal cells. For cerebellar cultures, the high cellular density limited whole-population analyses. Therefore, Purkinje neurons were selected to demonstrate that the proposed approach enables reliable spatial mapping of specific neuronal subtypes across the full well. Analyses were conducted at DIV14, as Purkinje neurons have been shown to reach an appropriate level of morphological and marker-expression maturity at this stage[23,24]. Purkinje cells were identified by calbindin fluorescence and manually annotated in ImageJ (Fig. 3F). We identified between 386 and 772 Purkinje neurons per well in the cerebellar cultures (Fig. 3G). In summary, we are able to detect cortical, hippocampal and cerebellar cells in automated fashion, or manually, thereby mapping cell distributions within neuronal networks in the cell culture dish.

Mapping spatial locations of neurons can be used to study neuronal organization in vitro

By detecting thousands of neurons and precisely mapping their spatial locations, we can quantitatively examine how different neuronal types from various brain regions self-organize within in vitro networks over time. In each well, the X and Y coordinates of every neuronal nucleus were recorded and used as cell centroids to measure intercellular distances. We first measured the distance of neurons from the center of the well to assess their spatial distribution (Fig. 4A). While neurons in general were spread evenly across the wells, especially hippocampal neurons and Purkinje cells tended to accumulate near the edges (Fig. 4A). We then calculated the intercellular
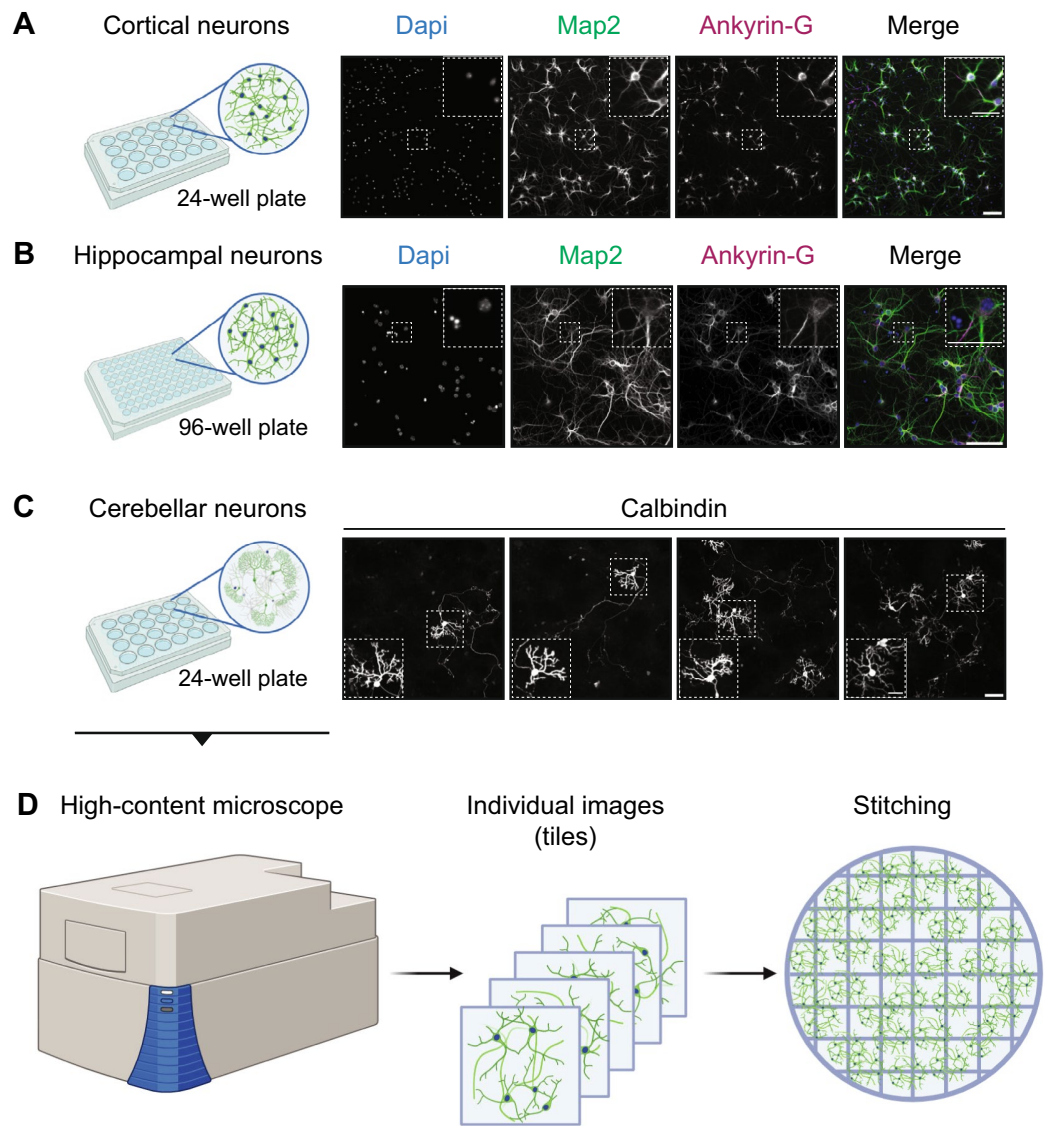
Fig. 1. Experimental and imaging workflow. (**A**) Primary mouse cortical neurons were plated on a 24-well plate and stained for Dapi (nucleus; blue), Map2 (soma and dendrites; green) and Ankyrin-G (axon initial segment; magenta). (**B**) Primary mouse hippocampal neurons were plated on a 96-well plate and stained as in A. (**C**) Primary mouse cerebellar neurons were plated on a 24-well plate and stained for calbindin (Purkinje cells, grey). (**D**) Plates were imaged on a high-content microscope. The individual confocal maximum intensity projection images (tiles) were then stitched together to yield a full-well image, where all individual cells plated in the well can be identified for downstream analysis. Images are maximum intensity projections of 5 stacks. Scale bars, 100 μm. Scale bars in the magnified insets, 50 μm.

distances between all neurons (Fig. 4B). Due to the finite well size, the maximum possible distance between cells is equal to the diameter of the well (~ 15 mm for a well in a 24-well plate, ~ 6,5 mm for a well in a 96-well plate). The distribution of intercellular distances exhibited a decline at larger distances, consistent with the circular geometry and boundary constraints of the wells. To minimize these boundary effects, we focused on neurons within the central region, located at half radius from the well center (Fig. 4C). Here, the cortical and hippocampal neuronal distributions reveal a small initial peak, followed by a gradual increase in neuronal density at greater distances. The accumulation of hippocampal cells at larger distances confirmed the edge accumulation observed in Fig. 4A. The initial peak is observed in all three neuronal cultures and at all time points, suggesting a distinct distribution of cells at short distances. To further investigate this initial peak, we examined the local density of cells within a maximum radius of 100 μm for cortical and hippocampal neurons, and of 500 μm for Purkinje cells (Fig. 4D). Cortical neurons showed a peak between 13 and 18 μm, with a maximum at 14 μm. Similarly, hippocampal neurons exhibited a peak between 12 and 20 μm, with the highest density between 13 and 16 μm. For Purkinje neurons, the analysis reveals a peak between 15 and 110 μm, with the highest density between 25 and 30 μm. This consistent peak in neuronal cultures suggests that neurons tend to remain close to one another,
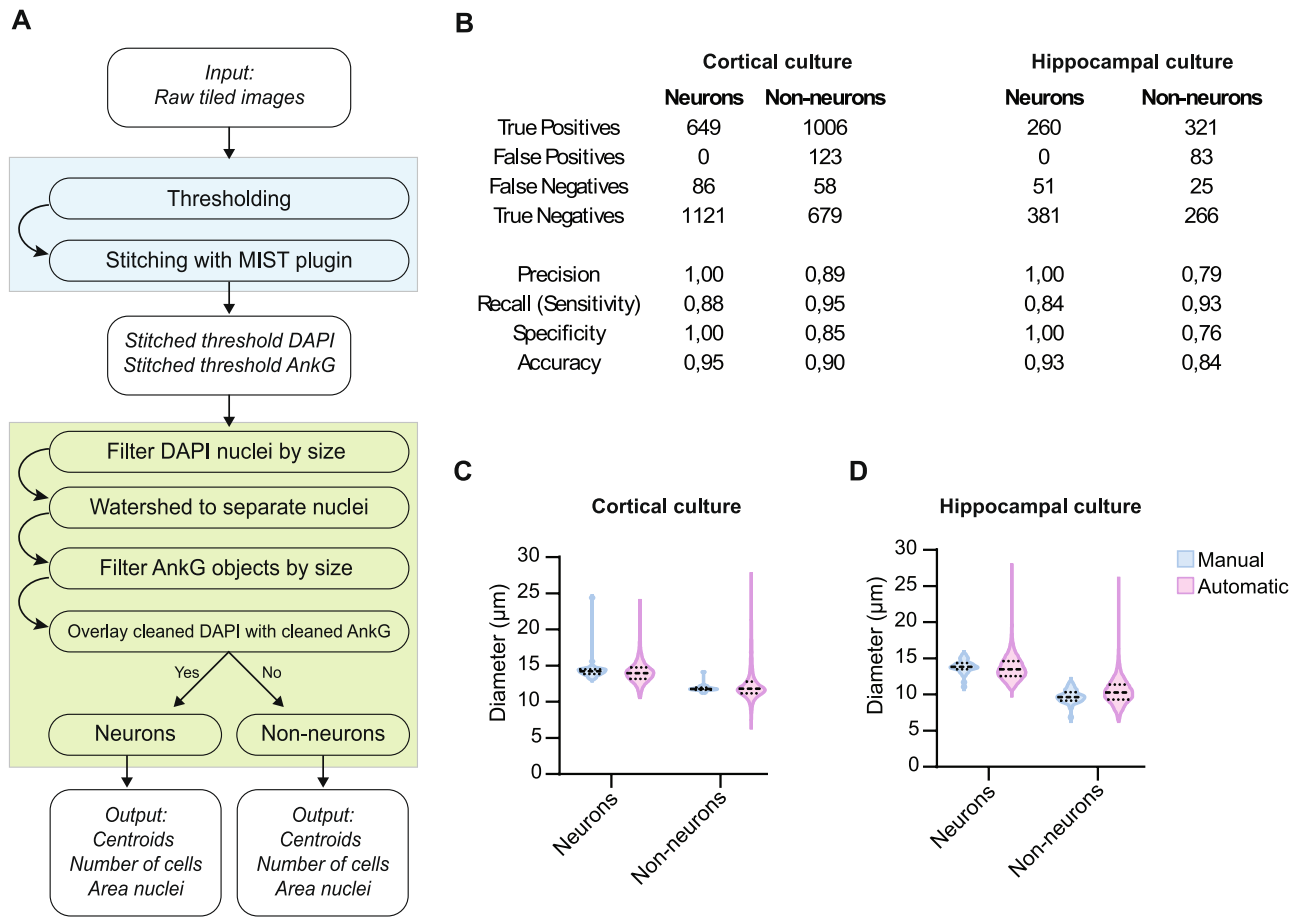
Fig. 2. Validation of the automated workflow for neuronal and non-neuronal cell classification. (**A**) Overview of the analytical workflow used for stitching and automated identification of neuronal and non-neuronal cells. (**B**) Confusion matrix summarizing the performance of the automatic classification compared to manual annotation in cortical (n = 1866) and hippocampal cultures (n = 695). (**C**) Comparison of nuclear diameters between manual (n = 30 cells) and automatic analyses in cortical cultures at DIV10. Mean ± SEM of neuronal cell diameter was 14.46 ± 0.35 μm (manual) and 14.00 ± 0.05 μm (automated); for non-neuronal cells, 11.80 ± 0.09 μm (manual) and 12.44 ± 0.07 μm (automated). (**D**) Same as C, but for hippocampal cultures. Mean ± SEM neuronal cell diameter was 13.83 ± 0.17 μm (manual) and 13.71 ± 0.01 μm (automated); non-neuronal cells measured 9.70 ± 0.17 μm (manual) and 10.44 ± 0.07 μm (automated).

likely forming pairs or small clusters during network formation. To evaluate whether these distance distributions could arise from random positioning alone, we generated a stochastic simulation of neuronal cells within a circular well. Random neuronal centroids were generated in MATLAB with a minimum-distance overlap rejection based on soma radius. Each simulation was matched to the experimental wells in terms of neuron number, soma diameter, and well radius. The simulated centroids were then analyzed using the same distance function as for the experimental datasets. Importantly, all the initial peaks were absent in random simulations (Fig. 4E), further supporting the observation of a preferred spacing between neurons. In line with these findings, we performed a cluster analysis at a critical distance of 20 μm, whereby cells separated by less than 20 μm were considered part of the same cluster. The frequency and cumulative frequency distribution analyses revealed a predominant cluster size of 2–3 cells, with a mean ± SEM of 2.32 ± 0.18 to 2.43 ± 0.36 in cortical neurons across the three DIVs (Fig. 5A,C), and 2.44 ± 0.12 to 2.59 ± 0.14 in hippocampal neurons (Fig. 5B,D). These results suggest the formation of small, spatially organized clusters. Compared with the random distribution, neuronal cells appear to have a higher tendency to form clusters. Overall, these analyses illustrate how spatial datasets enable detailed investigation of neuronal positioning and organization, opening the opportunity to more advanced studies of network architecture in vitro.

Non-neuronal cells in hippocampal and cortical cultures display no preferred intercellular distances

To assess the spatial organization of non-neuronal cells in our cultures, we also quantified the intercellular distances of these cells. In both cortical and hippocampal cultures, non-neuronal cells consistently accumulated near the well edges across all time points (Fig. 6A). Intercellular distance analysis of the full wells did not reveal any particular differences between neurons and the non-neuronal cells (Fig. 6B). Similar to the neuronal cell
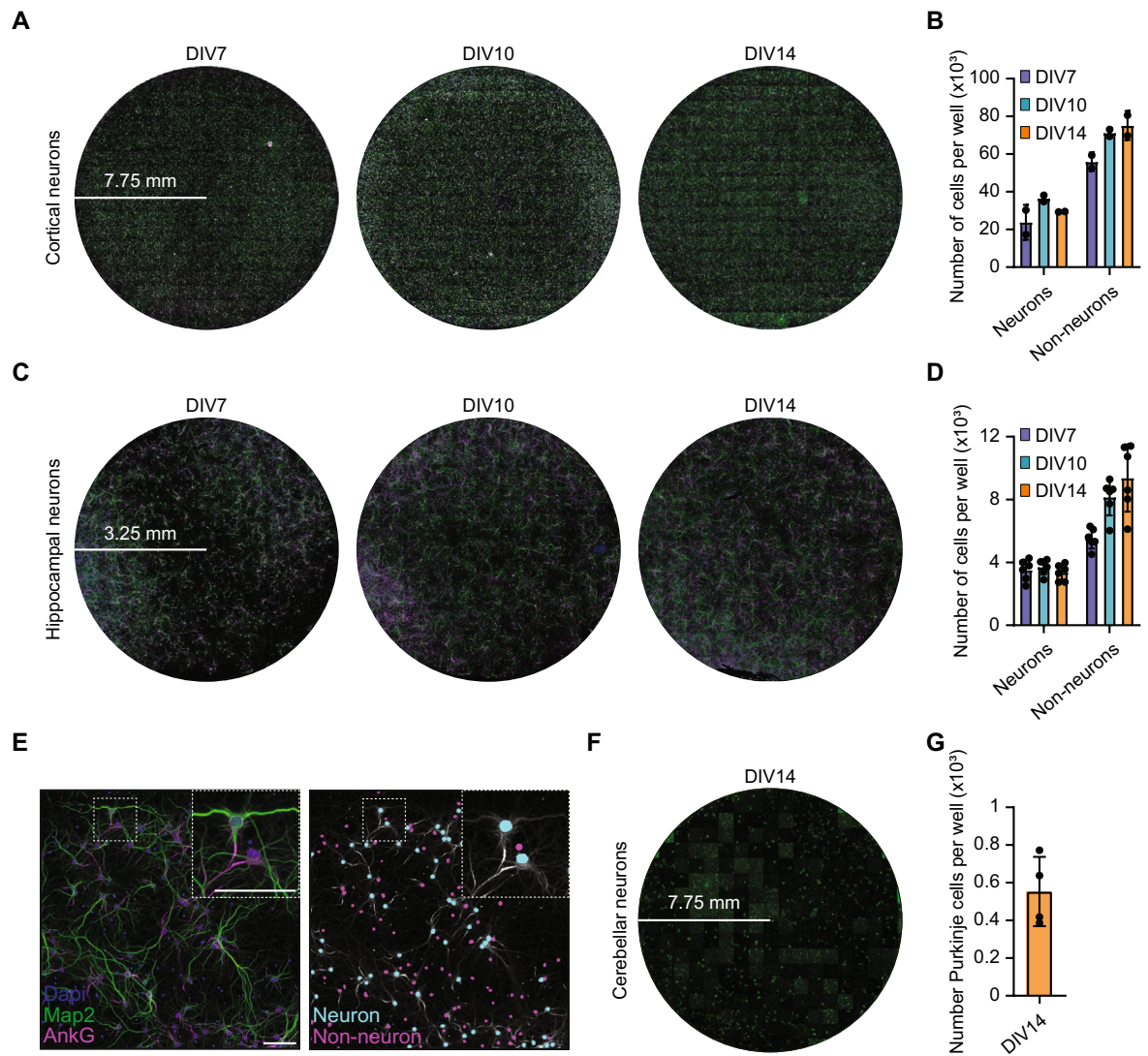
Fig. 3. Automated detection of all cells cultured in wells from different primary mouse neuronal cultures. (**A**) Representative image of a complete well of primary mouse cortical neurons at 7 (left), 10 (middle), and 14 DIV (right). (**B**) Number of neurons and non-neuronal cells per well at 7 (dark blue), 10 (light blue), and 14 DIV (orange). (**C–D**) Same as in A-B, but for primary mouse hippocampal neurons. (**E**) Representative image of primary mouse hippocampal neurons stained for Dapi (blue), the somatodendritic marker Map2 (green) and the axon initial segment marker AnkG (magenta) at 10 DIV (left). On the right, the same location showing the overlay of the Dapi and AnkG signals, after using our detection pipeline. Neurons are marked as cyan (detection of simultaneous Dapi and AnkG), and non-neuronal cells (only Dapi detected) are marked in magenta. Scale bar, 100 μm. Scale bar in the magnified inset, 50 μm. (**F**) Representative image of a complete well of primary mouse cerebellar cultures at 14 DIV, stained for calbindin (green). (**G**) Number of Purkinje cells (calbindin positive) per well. Each dot represents the number of neurons in one individual well. Data are represented as mean ± SEM. Data from 2, 6 and 4 independent wells per time point for cortical (N = 1), hippocampal (N = 2) and cerebellar cultures (N = 4), respectively.

analysis, we further focused on the central region of the well for the spatial distance analysis. In contrast to the neuronal cells, no distinct peak was observed in any of the non-neuronal cultures (Fig. 6C). The local density within a radius of 100 μm confirmed the absence of distinct peaks at short distances (Fig. 6D). A differential density plot comparing local distance distributions of neuronal and non-neuronal cells confirms distinct spatial organization patterns (Fig. 6E). The more prominent positive peak reveals that neuronal cells exhibit a clearer preferred intercellular distance at short range. These results suggest that, in contrast to neuronal cells, non-neuronal cells do not display a defined preferred spacing at short distances and instead tend to be more uniformly distributed within the culture dish.
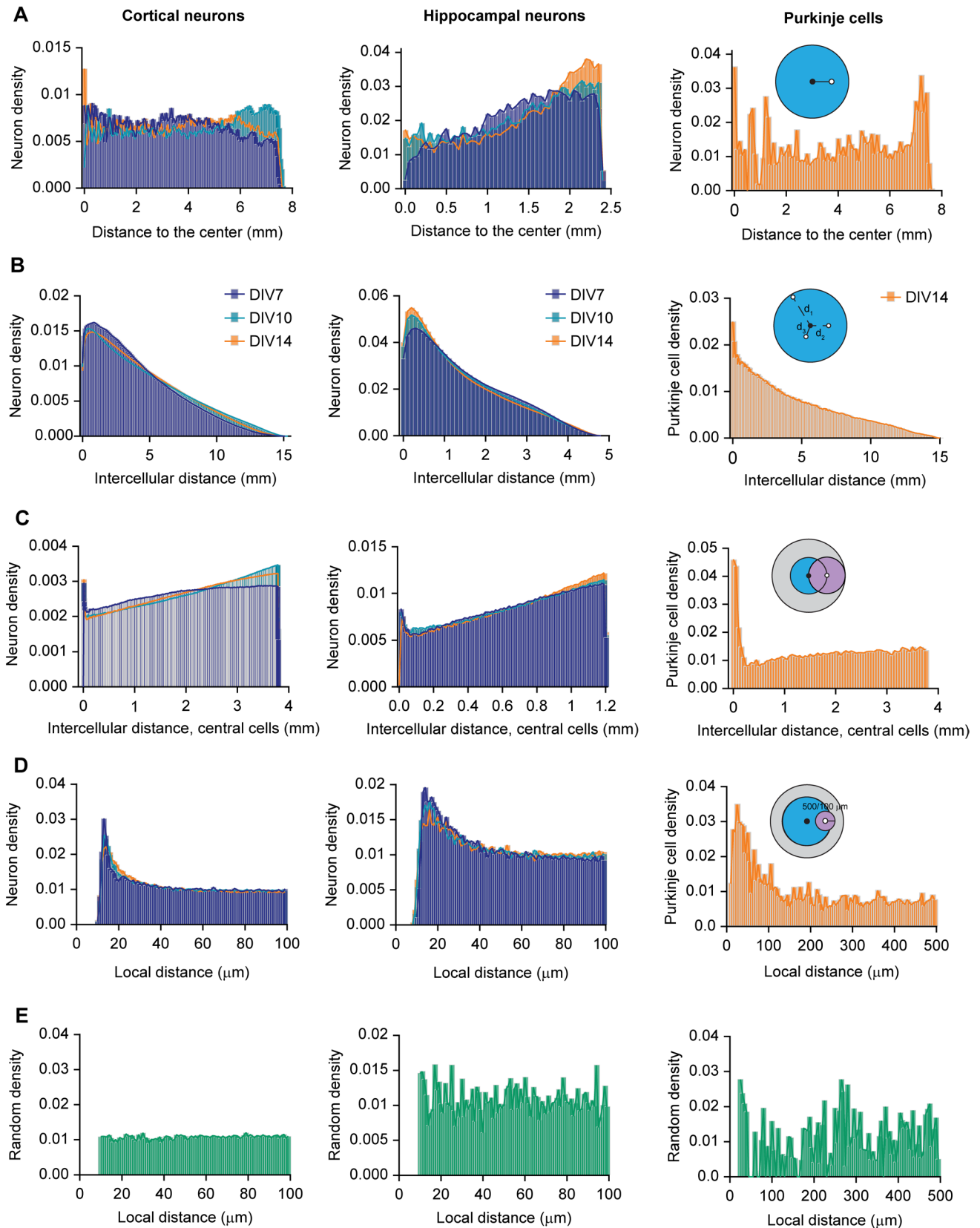
Insights into morphological details and cellular architecture from complete neuronal networks

To further demonstrate additional neuronal characteristics that can be obtained from analysing complete culture wells, we analysed the size of the nucleus[25], as well as the number and length of the axon initial segments identified in the dish[26]. For quantitative analysis of nuclear size of the large number of cells in our datasets, we automatically measured the nuclear diameters. Cortical neurons exhibited slightly larger nuclear diameters compared to non-

◀**Fig. 4.** Spatial analysis of the distribution of different mouse primary cultures shows a preferred distance between neuronal cells. (**A**) Distance of all neuronal cells to the centre of the well of cortical (left), hippocampal (middle) and Purkinje neurons (right) at 7 (dark blue), 10 (light blue), and 14 DIV (orange) normalized by the area and the total number of neuronal cells detected. Bin width is 50 μm for cortical and hippocampal neurons, and 100 μm for Purkinje cells. Schematic shows the area of the cells used for analysis (blue), a cell in the analysed area (white dot) and the black dot highlights the centre of the well. (**B**) Same as in A, but for the intercellular distance of all neuronal cells. Bin width equals 100 μm. Schematic shows 4 different cells (white dots), the distances between the cell in the centre of the well and the other three cells (dotted lines), and the area with cells used for the analysis (blue). (**C**) Same as in A, but for the intercellular distance between central neuronal cells. Cells at the periphery of the well were excluded. Bin width equals 10 (cortical and hippocampal neurons) and 50 μm (Purkinje neurons). Schematic shows the area of the cells used for analysis (blue), a cell at the periphery of the analysed area (white dot) and the area in which the distance is calculated for the particular cell (purple). The well area is shown in grey, and the black dot highlights the centre of the well. (**D**) Same as in C, but for the distance between local neurons. Local distance is defined as the distance between neurons within 10 to 100 μm radius from the analysed cortical and hippocampal neurons, or within 10 to 500 μm radius from the analysed Purkinje neuron. Bin width is 1 μm for cortical and hippocampal cultures, and 5 μm for cerebellar cultures. Statistical significance was assessed using the Kolmogorov–Smirnov (K–S) test and a permutation test (200 iterations) for all datasets, to evaluate deviations from random distributions, with p < 0.0001. (**E**) Local distance of random cells distributed in matching well area, cell size and cell density. Data from 2, 6 and 4 independent wells per time point for cortical (N = 1), hippocampal (N = 2) and cerebellar cultures (N = 4), respectively.
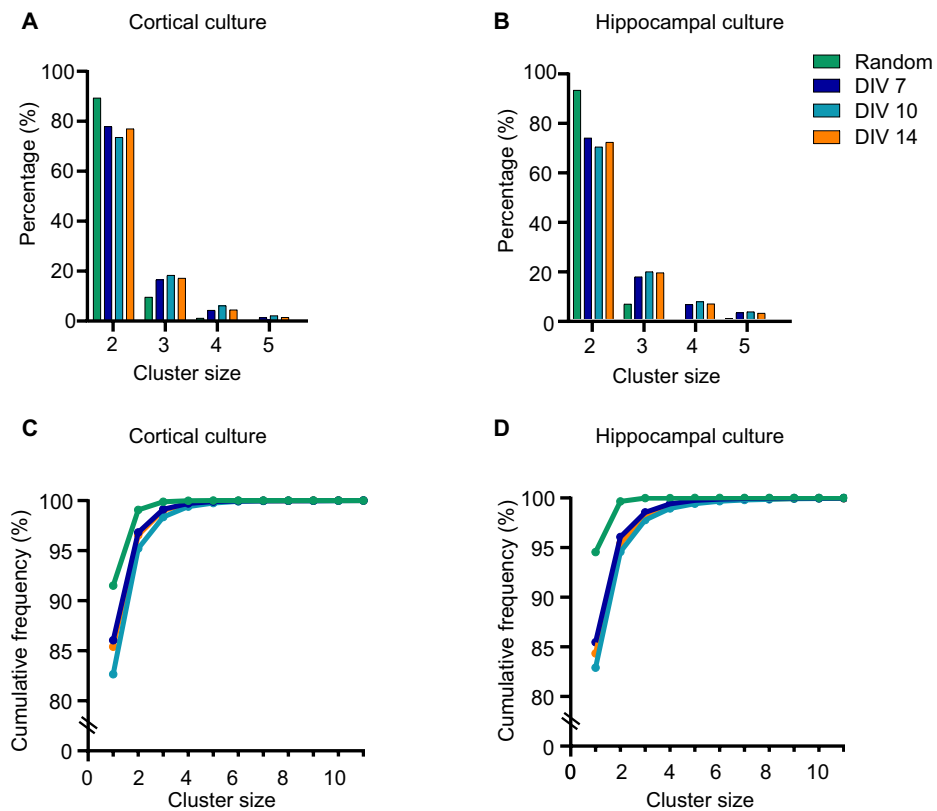

Fig. 5. Neuronal cells in primary cortical and hippocampal culture form small clusters. (**A**) Frequency distribution of the cluster size of neuronal cells in cortical culture and corresponding stochastic simulations. (**B**) Same as in A but for hippocampal culture. (**C**) Cumulative frequency distribution of the cluster size of neuronal cells in cortical culture and corresponding stochastic simulations. (**D**) Same as in C, but for hippocampal culture. Data from 2 and 6 independent wells per time point for cortical (N = 1) and hippocampal (N = 2) cultures, respectively.

neuronal cells, with a peak at ~ 14 μm and at ~ 12 μm, respectively (Fig. 7A,B). In the hippocampal cultures, a similar difference is observed, with a broader peak from 12–15 μm for neuronal cells, and a peak between 9 and 11 μm for non-neuronal cells. Of note, the nuclear diameter of hippocampal and cortical cells (Fig. 7A,B), corresponds with the preferred distance of the observed peak in the local distance analysis (Fig. 4D). This implies that hippocampal and cortical neurons indeed tend to cluster in a pair-wise fashion.
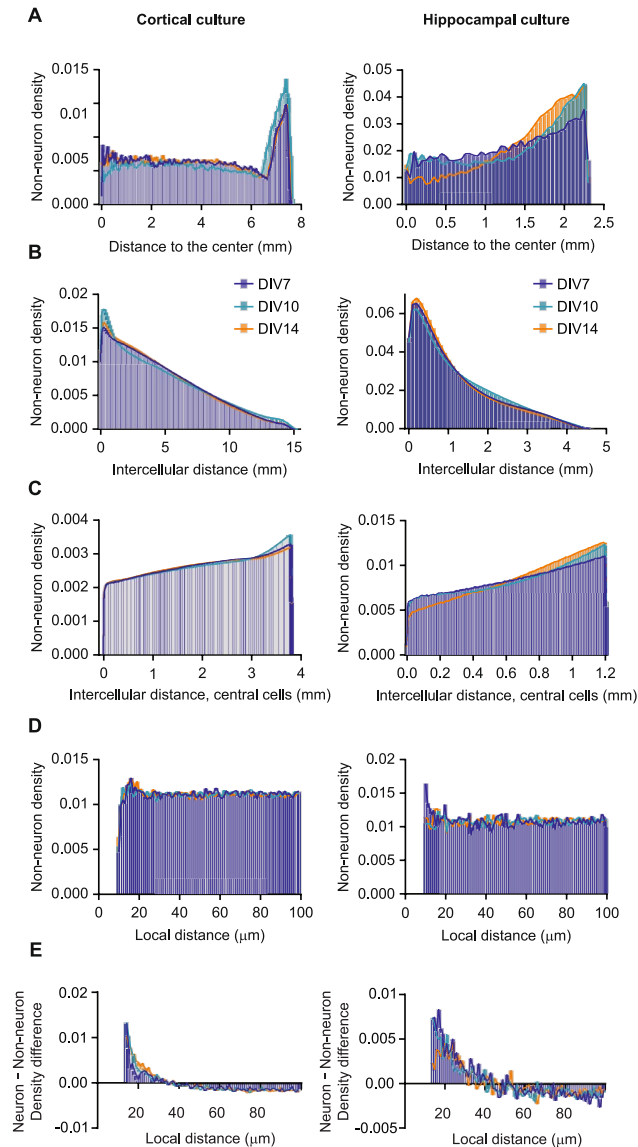
Fig. 6. Spatial analysis of the distribution of non-neuronal cells in primary mouse cortical and hippocampal cultures show no preferred distribution. (**A**) Distance between all non-neuronal cells (Dapi signal without overlapping AnkG) to the centre of the well at 7 (dark blue), 10 (light blue), and 14 DIV (orange) normalized by the area and the total number of cells. Bin width 50 μm. (**B**) Distance between all non-neuronal cells. Bin width 100 μm. (**C**–**D**) Same as in A, but for the intercellular distance between central non-neuronal cells (**C**), and for the distance between local non-neuronal cells (**D**). Bin width equals 10 μm (**C**) and 1 μm (**D**). (**E**) Differential density plot between local distance distributions of neuronal and non-neuronal cells. Bin width 1 μm. Data from 2 and 6 independent wells per time point for cortical (N = 1) and hippocampal (N = 2) cultures, respectively.

Our imaging setup is also compatible with available image segmentation tools such as Cellpose[27], which supports a workflow for self-training models. Here, we employ Cellpose to identify neurons based on DAPI and AnkG fluorescence, using the stitched image generated by our automated workflow described in Fig. 2. Neurons with a detectable axon initial segment (AIS) were segmented to assess AIS number, AIS orientation and AIS length across the complete in vitro network (Fig. 7C). Note that while this method provided useful insights, AIS detection accuracy was actually limited: a substantial number of neurons with an AIS were not recognized, particularly when the AIS was positioned further from the nucleus. As an example, we analysed one well of hippocampal cultures at DIV7, DIV10 and DIV14. Our data show that the large majority of detected neurons revealed a single AIS, while 10 to 17% displayed more than 1 AIS (Fig. 7D). Next, we examined whether the AIS showed a preferred orientation across the network by measuring their angles relative to the center of the well. No global orientation preference was observed (Fig. 7E). Finally, our analysis indicated that automatically measured AIS length reached up to 50 μm, with the mean ± SEM length of 12.7 ± 0.2 μm, 14.0 ± 0.3 μm and 16.1 ± 0.2 μm at DIV7, DIV10 and DIV14 respectively. Manual analysis of AISs length at DIV10 displayed a higher mean
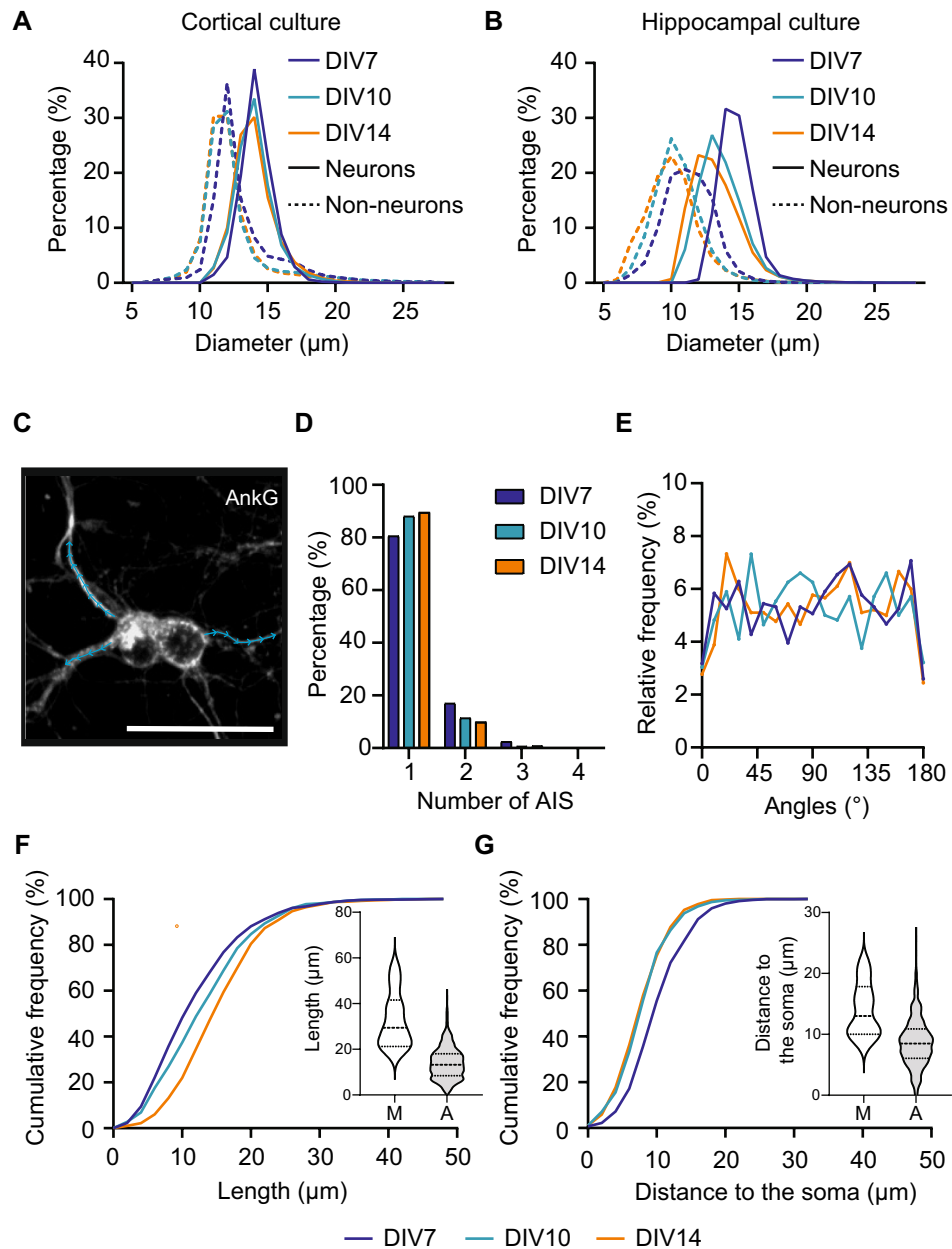
Fig. 7. Cell size and AIS analysis of a complete in vitro network. (**A**) Nuclei diameter of neuronal (full lines) and non-neuronal cortical cells (dashed lines) at 7 (dark blue), 10 (light blue), and 14 DIV (orange). (**B**) Same as A, but for hippocampal cells. (**C**) Representative image of AIS analysis of hippocampal neurons. Scale bar, 50 μm. (**D**) Percentage of AIS per neuron. (**E**) Angle relative to the center of the well of the AISs. (**F**) Cumulative frequency distribution of AIS length. Violin plots of manual (M, n = 10) and automatic (**A**) analyses of AIS length at DIV10 are shown. (**G**) Same as in F, but for the distance from the AIS center to the soma. Violin plots of manual (M, n = 10) and automatic (A) analyses of AIS-to-soma distance at DIV10 are shown. Data from 2 and 6 independent wells per time point for cortical (N = 1) and hippocampal (N = 2) cultures in (**A–B**), and from 1 well per time point (N = 1) in (**D–G**).

(32.66 ± 3.8 μm) (Fig. 7F), probably due to underrepresentation of long AISs in the automatic analysis. The geodesic distance of the AIS center (defined as the brightest AIS pixels) to the soma was typically around 10–15 μm. Manual analysis of the distance of the AIS to the soma was also around 14 μm at DIV10 (Fig. 7G). Together these results highlight just a few examples of possible applications of these large-scale datasets.

Discussion

How neurons develop and form cellular networks, both in vitro and in vivo, remains an intricate process that is not yet fully understood[8]. In this study, we present a pipeline for reconstructing, mapping and analysing complete primary neuronal networks in vitro. Combining high-content microscopy and automated analysis, entire cellular networks can be stained, imaged and reconstructed, enabling complete spatial characterization of the network. Our pipeline is versatile and applicable to multiple neuronal preparations, including cortical, hippocampal and cerebellar cultures, among others. Our pipeline is also well suited for "village-in-a-dish" experiments, in which cells from different donors are co-cultured[28]. This approach may enable the study of inter-individual variability in the more complete picture of cellular networks and provide insights on how genetic background shapes emergent network properties in the complete well.

Building on previous work demonstrating the reliability of high-content imaging (HCI) for neuronal quantification[29], our pipeline further enables parallel analysis of neuronal and non-neuronal populations, as well as the spatial distribution of cells within cultures, providing a more comprehensive view of in vitro network architecture. In addition, we show that HCI can resolve subcellular features with sufficient accuracy to quantify nuclear diameters of different cell types and AIS properties. Similar to soma size, reported to range from 15–20 μm in primary hippocampal cultures[30], this may serve as a classifier of cell populations[25]. AIS properties such as length (often reported as ~ 25–35 μm[31] with a peak intensity around 15 μm[32]), distance from the soma, number per neuron and orientation across the in vitro network reflect neuronal organization and subcellular heterogeneity, and alteration in AIS cytoarchitecture have been directly linked to both neurodevelopmental and neurodegenerative disorders[26,33]. Besides, the AIS has been shown to adapt to changes in neuronal activity, which has implications in neuronal functioning (reviewed in[34,35]).

Mapping all cell types within a culture dish, which our new pipeline achieves, provides an essential resource for more realistic in silico simulations of neuronal networks. Most in-depth computational models have focused on neuronal cells[36,37]. However, the well-established role of non-neuronal cells in modulating neuronal communication and network stability warrants detailed examination of their role on neuronal network formation as well[38]. Importantly, the inclusion of spatial information for both neuronal and non-neuronal populations might enhance the predictive value of such network models and offers new opportunities for algorithm training and machine learning approaches[39].

Understanding how healthy neuronal networks self-organize in vitro could provide a valuable reference for studying pathological alterations. For example, breakdown of small-world properties has been associated with Alzheimer's disease[40] and decrease in clustering coefficient is observed in an epilepsy model[41]. Our platform could, then, be used to compare cellular networks architecture in neuronal cultures prevenient from a healthy and a disease mouse model. Finally, our platform could be integrated into more classical drug screening studies in current high-content microscopy approaches, particularly in connectopathy-related disorders where altered neuronal connectivity and network organization are central features, offering a powerful readout for assessing drug efficacy.

All together, our new pipeline revealing the spatial organization of primary neuronal networks may provide novel insights into health and disease, and be utilized as a tool for developing novel therapeutics.

Limitations of the study

Neuronal classification in this study is based on AnkG immunolabeling, which enables highly specific identification of neurons with virtually no false positives. However, neurons with weak or absent AIS labeling may be misclassified as non-neuronal, reducing sensitivity. These cases mainly affect the total neuron count rather than the accuracy of spatial mapping.

Materials and Methods

Primary hippocampal and cortical neuronal cultures

Primary cortical and hippocampal neurons were prepared from embryonic day (E) 16.5 FvB/NHsD wild type mice according to the procedure described in[42] in compliance with the European Commission Council Directive 2010/63/EU (CCD project license AVD101002017893). Cortex and hippocampi were collected in cold Neurobasal medium (NB, Gibco). Tissues were incubated for 20 to 30 min in 0.05% trypsin/EDTA solution (Sigma Aldrich, T3924) at 37 °C. Cells were dissociated in NB supplemented with 2% B27 (Gibco), 1% glutamax (Gibco) and 1% penicillin/streptomycin(Sigma Aldrich). Cortical neurons were plated at a density of 50,000 cells/well onto 24-well plates (Nunc) and hippocampal neurons at a density of 12,500 cells/well on 96-well plates (Nunc) coated with poly-D-lysine (25 mg/mL, Sigma-Aldrich) in borate buffer (0.1 M prepared from Boric Acid, Sigma B0.252 and Borax, Sigma B9876) containing NB with supplements. The plates were incubated at 37 °C /5% CO_2 for 7, 10 or 14 days. Primary cortical cultures were prepared from pooled cortical tissue from multiple pups, with 2 wells analyzed per time point (biological N = 1). Primary hippocampal cultures were prepared from two individual pups, with 3 wells generated per pup, resulting in 6 wells per time point, biological N = 2).

Primary cerebellar neuronal cultures

Cerebellar neurons were prepared from postnatal day 1 (P1) wild type mice in compliance with the European Commission Council Directive 2010/63/EU (CCD project license AVD101002017893). Cerebella were isolated in ice-cold HBSS. The tissue was dissociated in trypsin (1 mg/mL; Sigma Aldrich, T5266) for 15 min at 37 °C, after which DNAase I (0.05 mg/mL; Merck, 10,104,159,001) was added and incubated for other 10 min. After adding 600 μl of Fetal Bovine Serum (FBS-12A, Capricorn Scientific), tissue was mechanically dissociated and centrifuged at 1000 rpm for 5 min. Cells were resuspended in Purkinje cells medium, composed of Neurobasal A medium (Thermo Fisher Scientific, 21,103,049) and the following supplements: 16 μg/ml putrescine (Sigma

Aldrich, P5780), 5 mg/ml sodium selenite (Sigma Aldrich, S5261), 13 mg/ml progesterone (Sigma Aldrich, P8783), 0.5 ng/ml tri-iodothyronine (Sigma Aldrich, T6397), 20 μg/ml insulin (Sigma Aldrich, I0516), 20 μg/ml apo-transferrin (Sigma Aldrich, T1147), 1% B27 Plus supplement (50x) (Thermo Fisher Scientific, A3582801), 1% GlutaMAX (Thermo Fisher Scientific, 35,050–061), and 1% Penicillin/Streptomycin (Thermo Fisher Scientific, P0781). Cells were plated at a density of $1.3–1.6 \times 10^6$/well on a 24-well plate (Garnier) coated with of 0.5 mg/mL poly-L-ornithine (Sigma Aldrich, P3655), containing Purkinje cell medium. The plates were incubated at 37 °C /5% CO_2 for 14 days and the medium was changed every 3 or 4 days. Primary cerebellar cultures were prepared from individual pups, with each well derived from a single pup (4 pups in total, N = 4).

Stainings

Neurons were fixed with 4% (w/v) paraformaldehyde (PFA; BosterBio)/ 4% sucrose (w/v) for 10 min at room temperature. After fixation, neurons were thoroughly washed three times for 5 min with $1 \times$ phosphate buffer saline ($1 \times$ PBS) and permeabilized with 0.2% Triton X-100 in PBS for 10 min. Cells were blocked with 5% normal goat serum (Life Technologies) and 0.05% Tween-20 in PBS for 30 min. Primary antibodies were applied overnight at 4 °C in blocking solution. After washing three times with $1 \times$ PBS for 10 min, cells were incubated with secondary antibodies in blocking solution for 1 h at room temperature. Once again, cells were thoroughly washed three times with $1 \times$ PBS for 10 min and kept in $1 \times$ PBS until imaging. Prior to imaging, the PBS of the wells was changed, and NucBlue Fixed Cell Stain (Dapi, 1:10; Invitrogen) was added to the cells.

The following primary and secondary antibodies were used: guinea pig ankyrin-G (1:500; Synaptic Systems, cat# 386 004, RRID:AB_2725774), rabbit Map2 (1:300; Cell Signaling, cat# 4542, RRID:AB_10693782), chicken calbindin D28k (1:1000; Synaptic Systems, cat# 214 006, RRID:AB_2619903), AlexaFluor 488 anti-rabbit (1:1000; Invitrogen, cat# A11008), AlexaFluor 488 anti-chicken (1:1000; Invitrogen, cat# a11008), AlexaFluor 568 anti-mouse (1:1000; Invitrogen, cat# A11004), AlexaFluor 647 anti-guinea pig (1:1000; Invitrogen, cat# A-21450) and AlexaFluor 488 anti-guinea pig (1:200; Jackson, cat# 706 545 148).

High-content confocal imaging and optical resolution limits

Images were acquired on the CellInsight CX7 LED High-Content Analysis Platform, in confocal mode, using a $10 \times$/0.30 NA objective (field of view: 877.8×877.8 μm; 1104×1104 px) for the cerebellar and cortical cultures or a $20 \times$/0.45 NA objective (field of view: 443.2×443.2 μm; 1104×1104 px) for hippocampal cultures, and the LED lines 386, 485, 560 and 640 (only for hippocampal cultures). Pinhole aperture was set to 70. Each image was a maximum intensity projection of 5 steps, each step of 5 μm with autofocus on DAPI channel at every image. Based on the Rayleigh criterion for diffraction-limited resolution ($d = 0.61 \times \lambda/NA$), the theoretical lateral resolution ranged from 0.66 μm (485 nm) to 0.88 μm (640 nm) for the $20 \times$/0.45 NA objective, and from 0.99 μm (485 nm) to 1.14 μm (560 nm) for the $10 \times$/0.30 NA objective. The corresponding image sampling was 0.401 μm/px for the $20 \times$ objective and 0.795 μm/px for the $10 \times$ objective. The resolution limits range from 1 to 2 pixels.

Although image acquisition in this study was performed using a CellInsight CX7 LED confocal platform, the analytical workflow is independent of specific hardware. Image stitching and analysis are based on open-source software (ImageJ/Fiji and Matlab) and could also be applied to image stacks acquired with other microscopes.

Image stitching

Image stitching was performed in two steps, using a set of macros for ImageJ. The first macro is to prepare the tiles for downstream stitching. Tiles names are converted from spiral grid into a column grid. The Li thresholding method was applied to all the channels[43]. After preprocessing, the tiles were stitched together using the Microscopy Image Stitching Tool (MIST)[44,45]. In these datasets, the MAP2 channel (for hippocampal and cortical datasets) or the DAPI channel (for cerebellar dataset) were used for the stitching. Estimated overlap was set to 2.0% and overlap uncertainty to 1.0%. The stitching tool outputs the stitched well image in RGB, the individual, the merged and the thresholded channels. To assess stitching precision, positional data provided by MIST were used to calculate residual displacements, defined as the difference between the observed and expected inter-tile offsets.

Nuclei and distance analysis

The analysis of the stitched wells was performed in MATLAB using a framework called Modular Image Analysis (MIA). MIA is divided into modules and uses parallel programming to analyze multiple wells simultaneously. The Nuclei Analysis module was used to differentiate between neuronal and non-neuronal cells. Cells were identified from the binary DAPI image, and objects outside the expected nuclear size range (50–950 px for $10 \times$ acquisition; 200–3800 px for $20 \times$ acquisition) were removed and the Watershed Algorithm[46] was applied to separate different nuclei. The binary AnkG image was similarly filtered to exclude objects smaller than the expected nuclear size. Next, the cleaned DAPI image was overlaid with the binary AnkG image to identify neuronal cells, with all other cells classified as non-neuronal. Classification performance was evaluated using three manually annotated tiles (1104×1104 px) from multiple wells for each DIV, generating a confusion matrix (Fig. 2B). Centroids of neuronal and non-neuronal cells were saved and used for the Distance Analysis module. For cerebellar neurons, centroids of the Purkinje cells were manually detected using the MultiPoint tool in ImageJ. The Distance Analysis module performed a spatial analysis of the distribution of cells in the wells. It calculated the distances between neurons and all other neurons using the pdist function from MATLAB. The distances of all the neuronal cells to the center were calculated by using the Euclidean Distance formula. The distance between central neurons was calculated by taking neuronal cells that are half the radius distant from the center, and the distance between local neurons was calculated within a radius of 100 μm or 500 μm for all neuronal cells more than 100 μm or 500 μm from the edges of the well. The same distances were calculated for non-neuronal cells. Random cell simulations were performed to provide a reference for comparison with experimental spatial organization. For each neuronal

type, a stochastic simulation of neuronal centroids was generated in MATLAB using random polar coordinates, which were then converted to Cartesian (X,Y) positions, combined with a minimum-distance overlap rejection based on soma radius. The simulation parameters were matched to the corresponding experimental wells: for hippocampal neurons, 3,500 neurons were simulated with a soma diameter of 14 μm inside a circular well with a radius of 3.25 mm; for cortical neurons, 30,000 neurons were simulated with a soma diameter of 14 μm inside a well with a radius of 7.75 mm; and for Purkinje neurons, 550 neurons were simulated with a soma diameter of 14 μm inside a well with a radius of 7.75 mm. The simulated centroids were then processed using the same distance function as applied to the experimental datasets.

Cluster analysis
Cluster analysis was performed in MATLAB using a neighbor-distance approach based on neuronal centroids and previously extracted intercellular distances. Neurons located within a critical distance of 20 μm were considered part of the same cluster. A connectivity graph was constructed, and connected components were identified using the conncomp function in MATLAB. The number of cells per cluster was recorded and used to generate frequency distributions of cluster sizes. The same analysis was performed on the random dataset.

Cellular feature analysis
To calculate the cell diameter, the measured cell area was used, assuming each cell to be a perfect circle. For the manual analysis, cell area was manually calculated in ImageJ and cell diameter was extracted assuming each cell to be a perfect circle. To analyze the axon initial segment (AIS), a customized Cellpose model[25] was trained to segment soma and AIS structures, using Ankyrin-G and DAPI images. Whole-well images were divided into overlapping 512×512 pixel tiles, segmented, and reassembled, with duplicate objects merged to generate unique identifiers. AIS detection and analysis were carried out in MATLAB. For each soma, candidate AIS objects were identified from the segmentation mask and Ankyrin-G channel, and filtered by size and circularity. AIS were validated based on Ankyrin-G intensity thresholds. The AIS center was defined as the most proximal high intensity pixel. Soma-to-AIS distances and AIS lengths were calculated using geodesic distance, defined as the shortest path along the segmented neuron mask between soma and AIS pixels. AIS trajectories were traced along the Ankyrin-G–positive structure, and orientation vectors were constructed. AIS angles were quantified by comparing the orientation of the terminal AIS vector with a reference vector pointing from each soma to the well center. AIS count, angles, AIS lengths and soma-to-AIS distances were extracted and converted to micrometers. The length of the axon initial segment (AIS) was measured manually using the segmented line tool in ImageJ. Intensity profiles were generated along the axon to determine AIS boundaries. The maximum fluorescence intensity within the AIS was identified from the profile, and the AIS starting point was defined as the first position where the intensity exceeded 30% of the maximum value. The distance to the soma was measured from the point of maximum intensity (AIS peak) to the beginning of the soma.

Statistical analysis
A two-sample Kolmogorov–Smirnov (KS) test was used to compare the overall distributions of real local neuron–neuron distances and corresponding random simulation distances. A permutation test (200 iterations) was performed to assess whether the proportion of short connections (≤ 20 μm for cortical and hippocampal datasets, or ≤ 110 μm for the cerebellar dataset) in the real data was significantly greater than expected by chance. All analyses were conducted in MATLAB (MathWorks).

Software
The following software was used in this manuscript: ImageJ (Version 1.54f.) (National Institutes of Health, USA; available at: http://imagej.org); MATLAB (Version R2021b) with Image Processing Toolbox (Version 11.4) (MathWorks; available at: https://www.mathworks.com); Anaconda (Conda Version 23.7.4) (Anaconda Inc.; available at: https://www.anaconda.com) and GraphPad Prism (Version 10.6.0) (GraphPad Software, LLC. Available at: https://www.graphpad.com).

Data availability
The datasets generated and analysed during the current study are available in the 4TU.ResearchData repository, at DOI: [https://doi.org/10.4121/08c1ce13-63d0-4950-bb0f-93fd72c894e0].

Code availability
The scripts and code used in this study are made available through Zenodo [https://doi.org/10.5281/zenodo.17555117].

References
1. Ramón y Cajal, S. *Histology of the Nervous System of Man and Vertebrates* (Oxford University Press, 1995).
2. Bullmore, E. & Sporns, O. The economy of brain network organization. *Nat. Rev. Neurosci.* **13**, 336–349. https://doi.org/10.1038/nrn3214 (2012).
3. Qiu, S. et al. Whole-brain spatial organization of hippocampal single-neuron projectomes. *Science* **383**, eadj9198 (2024).
4. Petersen, S. E., Seitzman, B. A., Nelson, S. M., Wig, G. S. & Gordon, E. M. Principles of cortical areas and their implications for neuroimaging. *Neuron* **112**, 2837–2853. https://doi.org/10.1016/j.neuron.2024.05.008 (2024).

5. Jun, S. et al. Organization of Purkinje cell development by neuronal MEGF11 in cerebellar granule cells. *Cell Rep.* **42**, 113137 (2023).
6. Watts, D. J. & Strogatz, S. H. Collective dynamics of 'small-world' networks. *Nature* **393**, 440–442 (1998).
7. Antonello, P. C. et al. Self-organization of in vitro neuronal assemblies drives to complex network topology. *Elife* **11**, e74921 (2022).
8. Schröter, M., Paulsen, O. & Bullmore, E. T. Micro-connectomics: Probing the organization of neuronal networks at the cellular scale. *Nat. Rev. Neurosci.* **18**, 131–146. https://doi.org/10.1038/nrn.2016.182 (2017).
9. Tlaie, A., Ballesteros-Esteban, L. M., Leyva, I. & Sendiña-Nadal, I. Statistical complexity and connectivity relationship in cultured neural networks. *Chaos Solitons Fractals* **119**, 284–290 (2019).
10. Yin, C. et al. Network science characteristics of brain-derived neuronal cultures deciphered from quantitative phase imaging data. *Sci. Rep.* **10**, 15078 (2020).
11. Südhof, T. C. The cell biology of synapse formation. *J. Cell Biol.* https://doi.org/10.1083/jcb.202103052 (2021).
12. Ballesteros-Esteban, L. M., Leyva, I., Almendral, J. A. & Sendiña-Nadal, I. Self-organization and evolution of structure and function in cultured neuronal networks. *Chaos Solitons Fractals* **173**, 113764 (2023).
13. De Santos-Sierra, D. et al. Emergence of small-world anatomical networks in self-organizing clustered neuronal cultures. *PLoS ONE* **9**, e85828 (2014).
14. Tibau, E., Ludl, A. A., Rudiger, S., Orlandi, J. G. & Soriano, J. Neuronal spatial arrangement shapes effective connectivity traits of in vitro cortical networks. *IEEE Trans Netw Sci Eng* **7**, 435–448 (2020).
15. Wilson, D. M. et al. Hallmarks of neurodegenerative diseases. *Cell* **186**, 693–714. https://doi.org/10.1016/j.cell.2022.12.032 (2023).
16. Hoffmann, C., Cho, E., Zalesky, A. & Di Biase, M. A. From pixels to connections: exploring in vitro neuron reconstruction software for network graph generation. *Commun. Biol.* https://doi.org/10.1038/s42003-024-06264-9 (2024).
17. Pegoraro, G. & Misteli, T. High-throughput Imaging as a versatile and unbiased discovery tool. *Methods* **96**, 1–2. https://doi.org/10.1016/j.ymeth.2016.01.003 (2016).
18. Garvey, C. M. et al. A high-content image-based method for quantitatively studying context-dependent cell population dynamics. *Sci. Rep.* **6**, 29752 (2016).
19. Aldewachi, H., Al-Zidan, R. N., Conner, M. T. & Salman, M. M. High-throughput screening platforms in the discovery of novel drugs for neurodegenerative diseases. *Bioengineering* **8**, 1–20. https://doi.org/10.3390/bioengineering8020030 (2021).
20. Hanamura, K. et al. High-content imaging analysis for detecting the loss of drebrin clusters along dendrites in cultured hippocampal neurons. *J. Pharmacol. Toxicol. Methods* **99**, 106607 (2019).
21. Mata, G. et al. Automated neuron detection in high-content fluorescence microscopy images using machine learning. *Neuroinformatics* **17**, 253–269 (2019).
22. Wæhler, H. A., Labba, N. A., Paulsen, R. E., Sandve, G. K. & Eskeland, R. ANDA: An open-source tool for automated image analysis of in vitro neuronal cells. *BMC Neurosci.* **24**, 56 (2023).
23. de Luca, A. et al. Distinct modes of neuritic growth in Purkinje neurons at different developmental stages: Axonal morphogenesis and cellular regulatory mechanisms. *PLoS ONE* **4**, e6848 (2009).
24. Alexander, C. J. & Hammer, J. A. Optimization of cerebellar purkinje neuron cultures and development of a plasmid-based method for purkinje neuron-specific, miRNA-mediated protein knockdown. *Methods Cell Biol.* **131**, 177–197 (2016).
25. Lingley, A. J., Bowbridge, J. C., Farivar, R. & Duffy, K. R. Mapping of neuron soma size as an effective approach to delineate differences between neural populations. *J. Neurosci. Methods* **304**, 126–135 (2018).
26. Huang, C. Y. M. & Rasband, M. N. Axon initial segments: Structure, function, and disease. *Ann. N. Y. Acad. Sci.* **1420**, 46–61. https://doi.org/10.1111/nyas.13718 (2018).
27. Stringer, C., Wang, T., Michaelos, M. & Pachitariu, M. Cellpose: A generalist algorithm for cellular segmentation. *Nat. Methods* **18**, 100–106 (2021).
28. Wells, M. F. et al. Natural variation in gene expression and viral susceptibility revealed by neural progenitor cell villages. *Cell Stem Cell* **30**, 312-332.e13 (2023).
29. Menduti, G. & Boido, M. Recent advances in high-content imaging and analysis in iPSC-based modelling of neurodegenerative diseases. *Int. J. Mol. Sci.* https://doi.org/10.3390/ijms241914689 (2023).
30. Peacock, J. H., Rush, D. F. & Mathers, L. H. Morphology of dissociated hippocampal cultures from fetal mice. *Brain Res.* **169**, 231–246 (1979).
31. Booker, S. A. et al. Input-output relationship of CA1 pyramidal neurons reveals intact homeostatic mechanisms in a mouse model of fragile X syndrome. *Cell Rep* **32**, 107988 (2020).
32. Freal, A. & Hoogenraad, C. C. Neuronal cytoskeleton: Presynaptic boutons as hotspots for activity-dependent microtubule nucleation. *Curr. Biol.* **29**, R1307–R1309 (2019).
33. Fujitani, M., Otani, Y. & Miyajima, H. Pathophysiological roles of abnormal axon initial segments in neurodevelopmental disorders. *Cells* https://doi.org/10.3390/cells10082110 (2021).
34. Fréal, A. *et al.* *Sodium Channel Endocytosis Drives Axon Initial Segment Plasticity*. https://www.science.org (2023).
35. Fréal, A. & Hoogenraad, C. C. The dynamic axon initial segment: From neuronal polarity to network homeostasis. *Neuron* **113**, 649–669 (2025).
36. Rubinov, M., Sporns, O., Thivierge, J. P. & Breakspear, M. Neurobiologically realistic determinants of self-organized criticality in networks of spiking neurons. *PLoS Comput. Biol.* **7**, e1002038 (2011).
37. Thivierge, J. P. Scale-free and economical features of functional connectivity in neuronal networks. *Phys. Rev. E Stat. Nonlinear Soft. Matter Phys.* **90**, 022721 (2014).
38. Manninen, T., Aćimović, J. & Linne, M. L. Analysis of network models with neuron-astrocyte interactions. *Neuroinformatics* **21**, 375–406 (2023).
39. Linne, M. L. Computational modeling of neuron–glia signaling interactions to unravel cellular and neural circuit functioning. *Curr. Opin. Neurobiol.* https://doi.org/10.1016/j.conb.2023.102838 (2024).
40. Ganbat, D., Jeon, J. K., Lee, Y. & Kim, S. S. Exploring the pathological effect of Aβ42 oligomers on neural networks in primary cortical neuron culture. *Int. J. Mol. Sci.* **24**, 6641 (2023).
41. Srinivas, K. V., Jain, R., Saurav, S. & Sikdar, S. K. Small-world network topology of hippocampal neuronal network is lost, in an in vitro glutamate injury model of epilepsy. *Eur. J. Neurosci.* **25**, 3276–3286 (2007).
42. Banker, G. & Goslin, K. Developments in neuronal cell culture. *Nature* **336**, 185–186 (1988).
43. Li, C. H. & Lee, C. K. Minimum cross entropy thresholding. *Pattern Recognit* **26**, 617–625 (1993).
44. Chalfoun, J. et al. MIST: Accurate and scalable microscopy image stitching tool with stage modeling and error minimization. *Sci. Rep.* **7**, 4988 (2017).
45. Blattner, T. *et al.* *A Hybrid CPU-GPU System for Stitching of Large Scale Optical Microscopy Images*.
46. Vincent, L. & Soille, P. Watersheds in digital spaces: An efficient algorithm based on immersion simulations. *IEEE Trans. Pattern Anal. Mach. Intell.s* **13**, 583 (1991).

Acknowledgements

Author contributions

Declarations

Competing interests

The authors declare no competing interests.

Ethical approval

All described experiments were ethically approved by the Erasmus MC. The study was conducted in accordance with the local legislation and institutional requirements and all methods were carried out in compliance with relevant guidelines and regulations.

Additional information

Correspondence and requests for materials should be addressed to D.H.M.

Reprints and permissions information is available at www.nature.com/reprints.

Publisher's note Springer Nature remains neutral with regard to jurisdictional claims in published maps and institutional affiliations.